



Using classical density functional theory to determine crystal-fluid surface tensions

Cédric Schoonen  and James F. Lutsko **Center for Nonlinear Phenomena and Complex Systems CP 231, Université Libre de Bruxelles, Blvd. du Triomphe, 1050 Brussels, Belgium*

(Received 20 June 2022; accepted 16 November 2022; published 7 December 2022)

Classical density functional theory is used to determine the fluid-solid surface tensions for low-index faces of crystals of hard spheres and Lennard-Jones particles. The calculations make use of the recently introduced explicitly stable fundamental measure theory model for hard spheres, and we show that this gives state-of-the-art accuracy compared to simulation. For the Lennard-Jones system, results are presented for both solid-liquid and solid-vapor interfaces, and in both cases the FCC results compare favorably with existing results from the literature. We find that the BCC crystal has significantly lower solid-liquid surface tension than the FCC structure. For the solid-vapor interface, our results indicate that the BCC phase is unstable with respect to transition to the HCP structure, in agreement with various zero-temperature results in the literature.

DOI: [10.1103/PhysRevE.106.064110](https://doi.org/10.1103/PhysRevE.106.064110)

I. INTRODUCTION

Surface tension is the fundamental controlling factor in a wide range of technological applications such as the crystallization [1], mechanical degradation of propellers (bubble cavitation [2]), wetting [3], and the design of super-hydrophobic surfaces [4] and the filling of pores (Cassie-Baxter to Wenzel transition [5]). The practical importance of these problems is hard to overstate. For example, in the case of crystallization, so-called “Disappearing Polymorphs”—where a carefully designed chemical process suddenly begins producing a different polymorph—is an increasingly important industrial problem [6]. This is critical, e.g., in pharmaceutical production, since the efficacies of pharmaceutical drugs often depend on the polymorph used (see, e.g., Refs. [7,8]). Indeed, drugs are patented and licensed for specific crystalline structures [9] making the control of polymorphism in their production a priority [10].

The calculation of bulk free energies has a long history, ranging from simple models such as the Lennard-Jones-Devonshire cell model [11] to more computationally demanding approaches such as liquid-state theory [12] and the most sophisticated modern techniques including quantum density functional theory [13]. Fluid-solid surface tensions are, however, much more difficult to determine since they involve density variations down to the molecular scale. Until recently, there has been no viable theoretical approach to the determination of general fluid-solid surface tensions, except in artificially idealized models: e.g., treating the solid as a structureless block or working at zero temperature, where only the interface with a vacuum has physical meaning (see, e.g., Ref. [14]). The state of the art has advanced significantly in the last 20 years with the maturation of classical density functional theory (cDFT), an approach to the description of inhomogeneous equilibrium systems that is based on the same

exact, theoretical framework of fundamental theorems as is the more familiar quantum DFT used in electronic-structure calculations [15–18]. Classical DFT can, in principle, be used to determine the equilibrium structure of inhomogeneous systems such as liquid-solid interfaces for any lattice-structure and crystal face. Unlike more heuristic approaches, such as phase-field crystal theory [19], cDFT is constructed from an intermolecular potential and as such give realistic results for, e.g., elastic properties of solids with various classes of interactions [20]. The introduction of provably stable functionals [21] has allowed its use to be extended even to highly inhomogeneous systems such as solid clusters in a fluid background [22,23].

Despite this promise, application of modern cDFT to the study of interfacial solid systems has so far been limited only to the special case of hard spheres [24]. This is partly because hard spheres have long played a central role in the formal and practical development of theory and partly because the most extensive simulation work has been done for hard spheres. Concerning the latter, the determination of the surface tension of the fluid-solid interface has proven very challenging as evidenced, e.g., by the history of this subject discussed in Ref. [25] and the fact that even today, values reported in the literature differ by 10% or more [24,25]. One of our goals here is to extend the use of cDFT to the more realistic and important case of small molecules interacting via a spherically symmetric pair potential: a much richer system possessing both liquid and vapor phases (as opposed to the single fluid phase in hard spheres) and which also serves as an effective model for colloids and macromolecules in solution.

In the next section, the cDFT framework is described: the particular models used in this study and the methodological adaptations necessary for its use to determine solid-fluid surface tensions. These are benchmarked for the important and highly nontrivial case of hard spheres where it is shown that our calculations reproduce prior work and new results are presented for the recently introduced explicitly stable fundamental measure theory model that forms the basis of our

*<http://www.lutsko.com>; jlutsko@ulb.ac.be

further applications. In Sec. III we present our results for the Lennard-Jones potential, considering in turn the liquid-solid interfaces and the vapor-solid interfaces for multiple crystal faces. We discuss a perhaps surprising instability of the BCC solid in contact with a vapor. The paper ends with a brief set of conclusions.

II. THEORY

A. Classical density functional theory

Classical DFT is a reformulation of some aspects of equilibrium statistical mechanics [16,17]. It primarily concerns the local number density $\rho(\mathbf{r})$ which is the same as the one-body distribution function and is based on theorems asserting the existence of a functional $\Lambda_\mu[\rho; \phi]$ of the local density, the chemical potential μ and any external field $\phi(\mathbf{r})$ acting on the system. This functional is a global minimum when evaluated at the density $\rho_\mu(\mathbf{r}; [\phi])$ corresponding to the equilibrium density generated by the external field. Furthermore, its value at this density, $\Lambda_\mu[\rho_\mu; \phi]$, is the grand-canonical free energy, $\Omega_\mu[\phi]$. Finally, the functional Λ can be written as

$$\Lambda_\mu[\rho; \phi] = F[\rho] - \int \rho(\mathbf{r})[\phi(\mathbf{r}) - \mu] d\mathbf{r}, \quad (1)$$

where the first term, $F[\rho]$, is called the Helmholtz functional and is independent of both the field and the chemical potential. In principle, knowing $F[\rho]$ would allow one, via minimization of Λ , to determine the equilibrium local density and grand-canonical free energy for any given external field.

In general, one does not know $F[\rho]$ except in certain special cases including the ideal gas and one-dimensional hard spheres (i.e., hard rods). For hard spheres, a great deal of work has led to a class of approximate functionals known as fundamental measure theory [18,26]. Our work uses a recent version of FMT called “explicitly stable FMT” [21] (esFMT) that gives a highly accurate description of the thermodynamics of the bulk hard-sphere solid. (For completeness, details of the functional are given in Appendix A.) For general spherically symmetric pair potentials $v(r)$, such as the Lennard-Jones potential, the potential is split into two parts, $v(r) = v_0(r) + w_{\text{att}}(r)$, where $v_0(r)$ is the short-ranged repulsive part of the potential and $w_{\text{att}}(r)$ is the long-ranged attractive part. The former is used to compute an effective hard-sphere diameter $d(T; [v_0])$ which, as indicated, depends on the temperature T , and the Helmholtz functional is approximated by

$$F[\rho] = F_{\text{HS}}(d(T; [v_0]), T; [\rho]) + \frac{1}{2} \int d\mathbf{r}_1 \int d\mathbf{r}_2 \rho(\mathbf{r}_1) \rho(\mathbf{r}_2) w_{\text{att}}(r_{12}), \quad (2)$$

where F_{HS} is the approximate esFMT hard-sphere functional. Further technical details of this model can be found in Appendix A.

All applications of cDFT involve the minimization of Eq. (1) with respect to the density to get the equilibrium local density and the total grand-canonical free energy of the system. Our calculations are performed by discretizing the local density on a rectangular computational grid consisting of $N_x \times N_y \times N_z$ points with lattice spacing Δ which was chosen so that there are about 20 points per hard-sphere diameter.

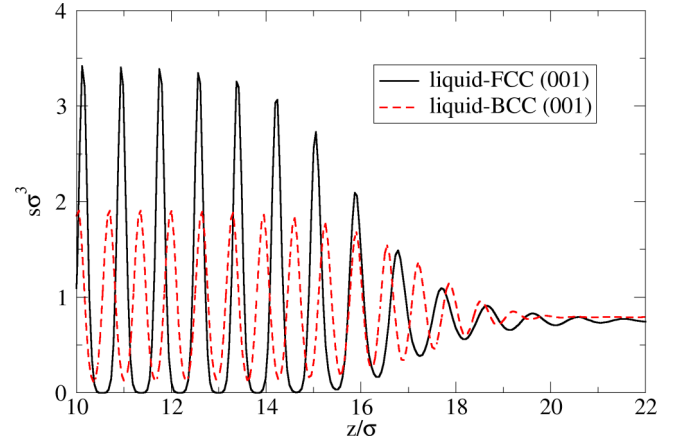


FIG. 1. Solid-liquid interfaces for both BCC and FCC Lennard-Jones solids (001) planes as determined from cDFT. The temperature is $k_B T = 1.0\epsilon$ where ϵ is the LJ energy scale and the length are scaled to σ , the LJ length scale [see Eq. (5)], which is the typical size of an atom or molecule. The figure shows the planar densities, i.e., the densities averaged over the planes perpendicular to the interface.

Periodic boundary conditions are applied in all directions and the codes implement the real-space formulation of FMT described in Lutsko and Lam [22] with the analytic FMT weights given in Ref. [27], where a discussion of the sensitivity to the lattice spacing can also be found. The attractive term in the free energy is evaluated simply by summing over the lattice sites efficiently using fast Fourier transforms. In this work, the external field $\phi(\mathbf{r})$ is always zero. The free energy functionals are then functions of the $N_x \times N_y \times N_z$ values of the density at the lattice sites and were minimized using the FIRE2 algorithm [28].

To determine the interfacial free energy between two phases, we work with a slab geometry with the z axis normal to the interfaces. The size of the computational cell in the x and y directions is determined by the dimensions of the unit cell of the solid while in the z direction, the length is approximately 50 molecular diameters giving on the order of 25 lattice planes of solid. By way of illustrating the results, Fig. 1 shows the planar densities, defined as

$$s(z) \equiv \frac{\int \rho(\mathbf{r}') \delta(z' - z) d\mathbf{r}'}{\int \delta(z' - z) d\mathbf{r}'} \quad (3)$$

for equilibrated FCC-liquid and BCC-liquid interfaces for a LJ system. A characteristic difference between the BCC and FCC structures is that the distribution of density around the Bravais lattice points has smaller amplitude and is broader for BCC than for FCC reflecting the less closely packed nature of the former. This is evidenced in the figure by the smaller, broader peaks of the planar density for the BCC than for the FCC away from the interface. The interface between the solid and liquid includes seven or eight lattice planes for BCC giving an interfacial width of about five molecular diameters and about 10 lattice planes for FCC giving a width of around nine diameters.

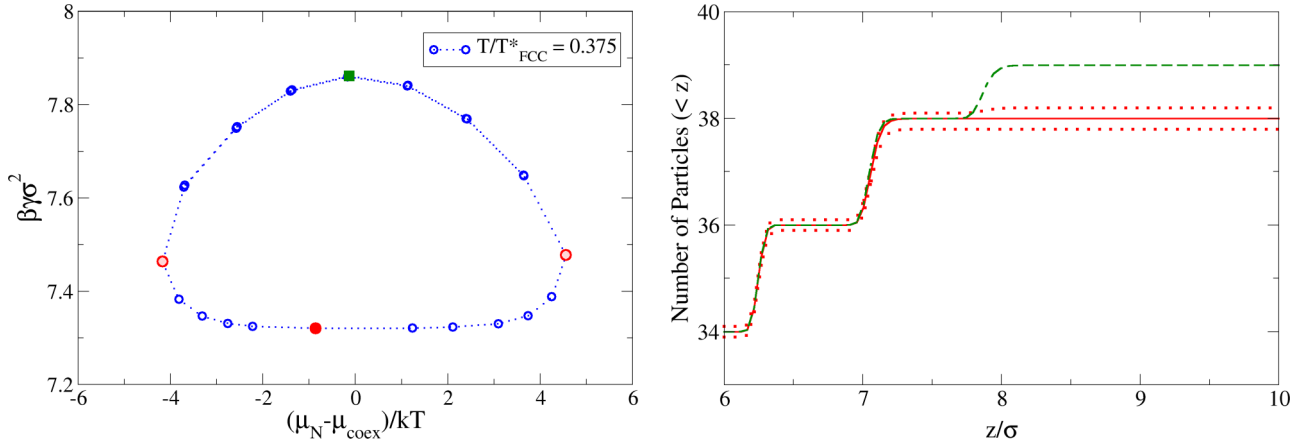


FIG. 2. Nonmonotonic evolution of the interfacial free energy as we change the number of particles. Here the interfacial free energy is that of a FCC solid exposing the (001) facet to the vapor. The temperature is $kT/\varepsilon = 0.3$, which corresponds to $T/T_{\text{FCC}}^* = 0.375$. The image on the left shows the interfacial free energy and supersaturation cycle as we change the number of particles in the system. (Each dot corresponds to a calculation with different numbers of particles.) The green square highlights a calculation with half-filled planes, while the red dots indicate calculations with almost complete planes. The large red dot in the middle (filled circle) is the closest to a complete plane, while the other two (open circles) are calculations with either a bit too much or too little mass to fill all the planes. The image on the right shows cumulative density profiles corresponding to these highlighted calculations. The red curves (plain and dotted) correspond to the red dots of the left image (filled and open, respectively) while the green curve (dashed) corresponds to the green square. Jumps between each plateau indicate the presence of a solid plane and the height difference between the plateaus indicate how many particles there are on that plane. The last plane at the interface is located at $z \approx 8\sigma$ and is partially filled depending on the number of particles in the calculation. The region beyond that interface ($z > 8\sigma$) is filled with the vapor which contains almost no particles, leading to a flat curve for the cumulative mass.

B. Determination of the interfacial free energy

For a (hypothetical) infinite system, one would simply set the chemical potential to the (known) value for coexistence, μ_{coex} , create some initial condition (e.g., a sharp interface between the two phases) and then minimize the cDFT functional $\Lambda_\mu[\rho, \phi = 0]$ to get the total free energy of the system. However, for a finite system, the coexistence properties are in general slightly different from that of the bulk systems so that minimizing at μ_{coex} results in one phase completely replacing another. In principle, one should then vary the chemical potential to find the (adjusted) coexistence value but this is difficult since it amounts to trying to find an unstable stationary point. It is more practical (but equivalent; see Appendix B 5 for details) to minimize the Helmholtz functional $F[\rho]$ at constant particle number, $N[\rho] = N_0$, with $N[\rho] \equiv \int_V \rho(\mathbf{r}) d\mathbf{r}$. For each value of N_0 , a stable interfacial system is found with a spatially constant chemical potential μ which is the coexistence chemical potential for the finite system.

To calculate the interfacial free energy, or surface tension [29], a Gibbs dividing surface is introduced to partition the total volume into the volumes of the two phases, V_1 and V_2 , via the requirements that $V_1 + V_2 = V$ and $\rho_1 V_1 + \rho_2 V_2 = N_0$, where $\rho_{1,2}$ are the bulk densities corresponding to the applied chemical potential μ and N_0 is the total number of particles in the relaxed interfacial system. The surface tension is then calculated as

$$\gamma = \frac{\Omega_\mu - \omega_{\mu,1}V_1 - \omega_{\mu,2}V_2}{2A} = \frac{F - f_1V_1 - f_2V_2}{2A}, \quad (4)$$

where A is the area of the interface and the grand potential per unit volume is $\omega_i = \Omega_i/V = f_i - \mu\rho_i$, etc., and f_i is the bulk Helmholtz free energy density for the phase i . One notes the key property of the Gibb's dividing surface is that the results

are the same using the canonical Helmholtz formulation and the grand-canonical formulation as is indicated in the second equality.

For a liquid-vapor interface, the surface tensions obtained are independent of the number of particles N_0 used in the interfacial calculation (as long as it is not too small or too large). Given an equilibrated interface, if one adds or subtracts a small amount of mass, the interface will simply move so as to have more or less of the denser phase, with no structural change to the interface nor any change to the densities far from the interface. As recently discussed by Maeritz and Oettel [30], this is not the case with a fluid-solid interface since the solid is not uniform: adding mass to the interface results in a partial solid plane which will have a higher free energy than a fully constructed plane. So, if mass is added to an equilibrated solid-fluid interface and then the system is relaxed, the added mass may end up as a partially filled plane, an increase of bulk solid or fluid densities or some combination of both.

Consequently, when performing calculations using a *finite* system, there is no unique interfacial free energy for the solid but rather a periodic variation as a function of N that returns to a minimum value each time a complete crystal plane is formed; see Fig. 2, where each point is a result of adding mass and then relaxing while holding the cell dimensions fixed in all directions (hence, constant lattice parameter in the directions perpendicular to the interface). This means that, in the finite system, there is no unique excess surface free energy. (Alternatively, it means that the state of the system can only be specified by introducing an additional variable characterizing the completeness of the last solid plane—a variable that would have a fixed value in the thermodynamic limit and, hence, would become irrelevant.) However, in an infinite system, it is clear that any added mass would be absorbed into the fluid

TABLE I. Fluid-solid interfacial and coexistence properties for the hard-sphere system. The physical quantities reported in the table are the fluid and solid densities, the pressure, the chemical potential, and the fluid-solid interfacial free energies for multiple faces of the FCC solid, except for the last two rows reporting cDFT results for BCC. The rows reporting values from this work are marked by an asterisk. The results of Davidchack *et al.* are taken from [25] and those of Oettel *et al.* from [24].

Source	$\rho_f \sigma^3$	$\rho_s \sigma^3$	$\beta P \sigma^3$	$\beta \mu$	$\beta \gamma_{(001)} \sigma^2$	$\beta \gamma_{(110)} \sigma^2$	$\beta \gamma_{(111)} \sigma^2$
WBII (Oettel <i>et al.</i>)	0.945	1.039	11.87	16.38	0.69	0.67	0.64
WBII ($\Delta \approx 0.0125\sigma$)*	0.946	1.039	11.94	16.46	–	–	–
WBII ($\Delta \approx 0.025\sigma$)*	0.950	1.041	12.16	16.68	0.69	–	–
WBII ($\Delta \approx 0.05\sigma$)*	0.966	1.046	13.09	17.65	0.71	–	–
esFMT ($\Delta \approx 0.05\sigma$)*	0.942	1.027	11.96	16.50	0.51	0.47	0.46
Sim. (Davidchack <i>et al.</i>)	0.940	1.041	–	–	0.58	0.56	0.54
Sim. (Oettel <i>et al.</i>)	0.938	1.039	–	–	0.63	0.61	0.60
BCC WBII (Turci <i>et al.</i> [31])	1.016	1.045	–	–	0.34	0.33	0.32
BCC esFMT ($\Delta \approx 0.05\sigma$)*	0.967	1.008	13.45	18.06	0.21	0.20	0.20

leaving the interface in the minimum energy (i.e., complete lattice plane) state. We therefore use the minimum value on this curve to define the surface tension for the corresponding value of chemical potential. Further justification for this procedure is given in Appendix B 6 b where it is shown that this gives the best estimate of the value at coexistence and here it is simply noted that in the thermodynamic limit the fluid volume becomes infinite and any finite added mass can go into the fluid phase, neither changing the structure of the interface nor the supersaturation.

C. The paradigmatic test case: Hard spheres

The hard-sphere system is the only one for which we found cDFT results in the literature using modern cDFT functionals and unconstrained minimizations: Oettel *et al.* [24] used the White Bear II (WBII) model cDFT functional [32] to calculate liquid-solid interfacial energies for several crystalline planes. To validate our codes and procedures, they were used to perform the same calculation, with the same functional, for the (001) face of an FCC crystal, and the results given in Table I are in good agreement with theirs. This comparison was further used to benchmark the sensitivity of the calculations to computational details such as grid spacing, etc. Finally, and most relevant to the present work, results are given for the recently proposed esFMT hard-sphere model as well as recent simulation results. One observes that the results using both cDFT functionals are of similar quality compared to simulation, with the difference however that the esFMT results are generally lower than the simulation values, whereas the WBII results are higher. Qualitatively, the ordering $\gamma_{(111)} < \gamma_{(110)} < \gamma_{(001)}$ of crystal faces according to the interfacial free energy is consistent in all cases considered. Note, however, that this differs from the naive expectation that interfacial free energy is inverse to the planar density: for FCC, the ordering by planar density is $s_{(111)} > s_{(100)} > s_{(110)}$. This is because the

surface free energy also depends on the nontrivial structure of the fluid near the interface: the planar density is expected to be the dominant factor only for interfaces with a vacuum (or low-density vapor). Quantitatively, the difference of 10% to 20% between cDFT and simulation results should be contrasted with the significant variation between simulation results recently reported in the literature, which is at least half this range. This comparison shows that for interfacial properties, the esFMT model is competitive with the widely used WBII functional, which is in accord with previous work concerning thermodynamics [21]. Finally, recall that there is no question of FCC-BCC polymorphism in hard spheres because the BCC phase is unstable to shear [33].

III. INTERFACIAL PROPERTIES OF THE LENNARD-JONES SOLID

A. Lennard-Jones potential

Our calculations are based on the Lennard-Jones potential with energy scale ϵ and length scale σ ,

$$v_{LJ}(r) = 4\epsilon \left[\left(\frac{\sigma}{r} \right)^{12} - \left(\frac{\sigma}{r} \right)^6 \right], \quad (5)$$

which has been used in a large body of literature as a prototypical small-molecule potential and as a basis for modeling both noble gases and metals. However, the LJ potential is almost never used in this form: for practical reasons, its range is truncated at some cutoff distance, r_c , and it is shifted giving $v(r) = v_{LJ}(r) - v_{LJ}(r_c)$ for $r < r_c$ and zero otherwise. For molecular dynamics simulations, it is often further modified so that its first derivative, the force, also goes smoothly to zero at the cutoff with the most notable example of this kind of modification being that of Broughton and Gilmer [34] which is

$$v(r) = \begin{cases} v_{LJ}(r) + C_1, & r \leq 2.3\sigma \\ C_2 \left(\frac{\sigma}{r} \right)^{12} + C_3 \left(\frac{\sigma}{r} \right)^6 + C_4 \left(\frac{\sigma}{r} \right)^{-2} + C_5, & 2.3\sigma \leq r < 2.5\sigma \\ 0, & 2.5\sigma \leq r \end{cases} \quad (6)$$

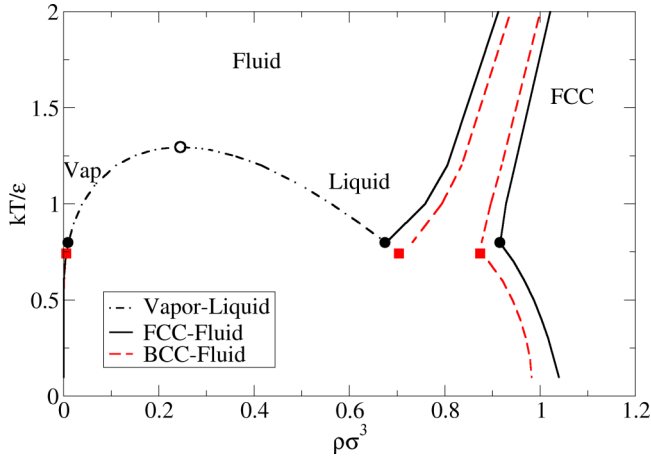


FIG. 3. Phase diagram of the Lennard-Jones potential showing coexistence lines for both the FCC and BCC solid as calculated using our cDFT model. The liquid-vapor critical point is shown as an open circle, the vapor-liquid-FCC triple point is shown as filled circles, and the vapor-liquid-BCC triple point as filled squares

with $C_1 = 0.016132$, $C_2 = 3136.6$, $C_3 = -68.069$, $C_4 = -0.083312$, $C_5 = 0.74689$. (The sign of C_4 is incorrectly reported as positive in the original publication.)

The cDFT model, with its mean-field treatment of the long-ranged part of the potential, is not designed to be quantitatively accurate and so not attempt was made to reproduce any particular study. This work uses the simple cutoff and shifted version of the LJ potential with $r_c = 3\sigma$ (consistent with our previous work [23,27]).

Unlike the hard-sphere interaction, LJ systems exhibit the standard vapor-liquid-solid phase diagram (see Fig. 3) and the calculated values of the critical and triple points are given in Table VI in the Appendixes. For LJ, the minimum free energy solid phase is either FCC or HCP, depending on the conditions [35], but there is little difference between their free energies [27]. We chose to work with the FCC phase out of convenience and because there are more simulation results for this phase. Unless otherwise stated, these and all reported results are for a computational grid spacing of 0.05σ .

In the following, our results are compared to simulations, where possible, and to reduce the effect of differences in details of how the potential is cut off [36] the temperature was scaled to the triple point temperature (for FCC or BCC as appropriate and denoted T_{FCC}^* and T_{BCC}^* , or generically T_{XCC}^*) determined from the underlying method (e.g., cDFT or simulation). The point of the comparisons is thus not to show quantitative correspondence but just to note that, when such comparisons are possible, the cDFT results are physically plausible.

In the following, reference is also made to “exact” zero-temperature calculations. What is meant by this is simply that molecules are treated as point particles and the total energy evaluated as $U = \frac{1}{2} \sum_{i \neq j} v(r_{ij})$ for the relevant configuration: i.e., a crystal slab adjacent to a vacuum in order to calculate the surface tension. In bulk calculations, the dimensions of the periodic box are relaxed to give a minimum of the energy U . The solid-vacuum interfacial free energies are computed using a box with the bulk solid dimensions and periodic boundary

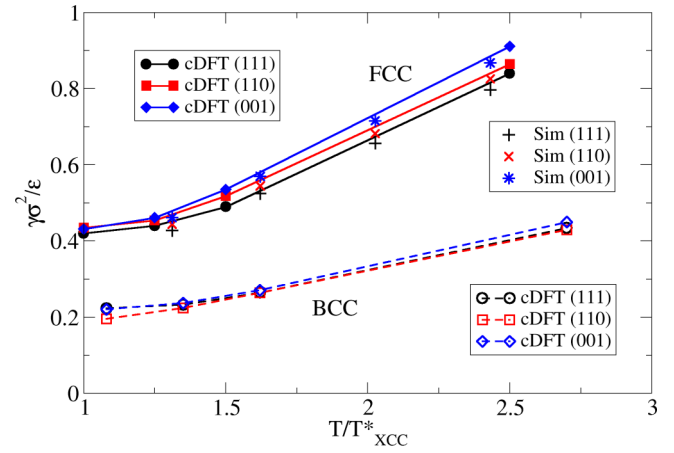


FIG. 4. Interfacial free energies for the liquid-solid coexistence in simple fluids. The temperatures are scaled using the corresponding triple point temperature: T_{FCC}^* or T_{BCC}^* . The simulation data comes from Laird *et al.* [37]. Error bars are a bit smaller than the symbols, not taking the finite spacing Δ into account (see Appendix E for details).

conditions in the x and y coordinates. The periodicity in the z direction is removed to emulate the interface with a vacuum. The molecular positions and dimensions of this solid slab are in most cases fully relaxed (see Appendix C for a full explanation).

B. Solid-liquid interfaces

The surface free energies from our calculations for solid-liquid interfaces are shown in Fig. 4. For the FCC phase, the ordering of the surface tensions is $\gamma_{(111)} < \gamma_{(110)} < \gamma_{(001)}$, the same as found for hard spheres above. Note however that the difference between the surface tensions goes to zero near the triple point and grows as the temperature increases, although it is never very large in the range of temperatures considered here. The figure also includes simulation data from Laird *et al.* [37] and shows that the values obtained are physically reasonable.

For the BCC phase, one sees that at all temperatures the interfacial free energy is roughly half that of the FCC phase, suggesting that the BCC structure is energetically more favorable than FCC for small clusters, which is a point discussed in greater detail in the next section. The BCC values show very little difference between the different crystal planes, although one can say that $\gamma_{(110)} < \gamma_{(111)} < \gamma_{(001)}$ which, as for FCC, is different from the planar densities which now order the planes as $s_{(110)} > s_{(100)} > s_{(111)}$. To our knowledge, there are no studies reporting liquid-BCC interfacial free energies from simulation.

C. Solid-vapor interfaces

Interfacial free energies for FCC solid-vapor interfaces are shown in Fig. 5 together with simulation results. In the previous section, we described the finite-size effects resulting in nonmonotonic behavior of the free energy as incomplete crystal layers are constructed. This is discussed in detail in Appendix B 6 b, but here it is noted that this effect is stronger

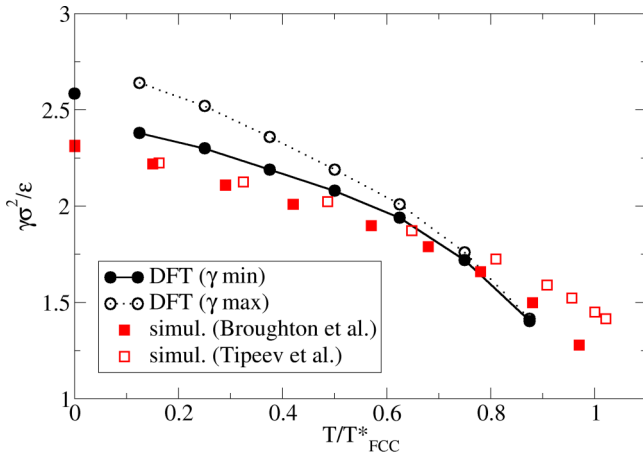


FIG. 5. Interfacial free energies for the vapor-FCC solid coexistence in simple fluids, exposing the (001) plane. The temperatures are scaled using the corresponding triple point temperature T_{FCC}^* . The simulation data come from [34] and [38]. The filled and open circles are the cDFT minimal and maximal surface tensions, as discussed in the text, except at zero temperature where the exact results are shown. Error bars are a bit smaller than the symbols, not taking the finite spacing Δ into account (see Appendix E for details).

for the the solid-vapor interface than for the liquid-vapor interface. In the figure, the magnitude of the effect is illustrated by showing both the minimum and the maximum values of surface free energy resulting from it. The minimum values—which are the physically relevant ones corresponding to complete crystal planes—are again in reasonable agreement with the available simulation values showing they are physically reasonable, although the temperature dependence of the cDFT results are somewhat stronger near the triple point than observed in simulation. The simulation data comes from two references that use different techniques. The group of Broughton *et al.* [34] pioneered the calculation of interfacial free energies in the 1980s using indirect methods; they obtain γ by computing the surface entropy by thermodynamic integration from zero-temperature approximations. In contrast, the recent results from Tipeev *et al.* [38] are computed with the more direct crystal cleavage method. These two results—the only ones for the vapor-solid interface that we are aware of in the literature—differ significantly at higher temperatures illustrating the difficulty of obtaining this information. Finally, also shown in the figure are exact zero-temperature values. As seen in Fig. 5, our results are not as consistent with these the zero-temperature values, but this is likely due to the finite size of the computational grid, as supported by the fact that when the grid spacing is decreased from $\Delta \approx 0.05\sigma$ to $\Delta \approx 0.025\sigma$, the difference between the zero-temperature limit of cDFT calculations decreases by a factor 2 (see Table VII in the Appendixes).

Surface free energies for several planes of low Miller index are given in Fig. 6. Calculations were also performed for the BCC phase but there are a number of complications in this case. While the (001) face presented no problems, when we attempted to equilibrate the (110) and (111) BCC-vapor interfaces we found that the entire BCC lattice was distorted; see Fig. 7. Recall that these calculations are performed in a

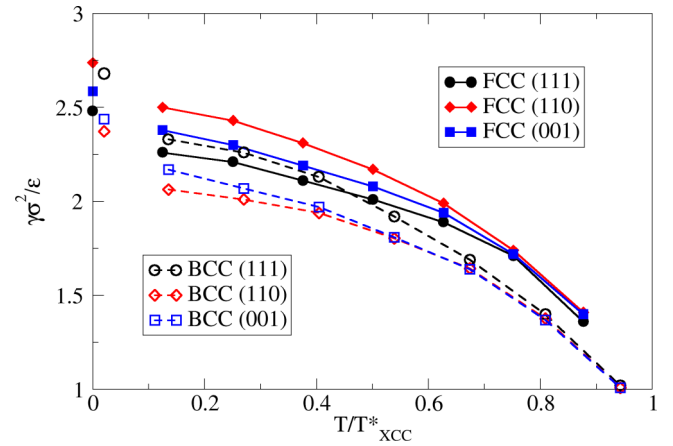


FIG. 6. All interfacial free energies (FCC and BCC) for the vapor-solid coexistence in simple fluids. The temperatures are scaled using the corresponding triple point temperature: T_{FCC}^* or T_{BCC}^* . The finite temperature values are from cDFT and the zero-temperature values are the exact calculations. Note that the zero-temperature calculations for BCC are offset on the temperature axis, for clarity. Error bars are a bit smaller than the symbols, not taking the finite spacing Δ into account (see Appendix E for details).

cell with periodic boundaries in the directions parallel to the interface so that the system is symmetry-constrained and this presumably explains why no such distortion was observed when using the (001) BCC crystal face. It might be thought that this apparent instability is a consequence of the fact that the cDFT functional is based on a hard-sphere functional and that hard spheres are well known to be unstable in a BCC configuration. To explore this further, we performed exact zero-temperature calculations for a BCC (110) crystal face in contact with a vacuum to which a small amount of noise was added to the molecular positions. We again found that the BCC structure was not stable but rather deformed via a sliding of the (110) plane (more details are given in Appendix C). In Fig. 8 we show that the BCC structure in contact with a vapor (or vacuum at zero temperature) is in fact fully unstable (as opposed to metastable) to this distortion: the energy decreases monotonically as small displacements of the (110) plane are made. (Note that by symmetry, one expects that the BCC structure is a stationary point—and so a local maximum—of the free energy.) Furthermore, we find that if we relax a fully periodic BCC crystal (after adding a small amount of noise to the system) while allowing the shape of the periodic cell to change, the system always deforms to an HCP structure, regardless of the amplitude of the noise.

These observations change as a function of the computational grid spacing. For coarser lattices (e.g., $\Delta = 0.2\sigma$), the possible displacements of the (110) plane are larger and the minimum in the free energy is not observed, as evidenced in Fig. 8. Indeed, the equilibrium shift of the (110) plane is on the order of 0.1σ which is thus smaller than the computational grid spacing in this case and so inaccessible. Nevertheless, when we try to relax a (110) interface on the coarser lattice, a distortion of the bulk is observed, an example is shown in Fig. 7, albeit somewhat different from that seen on the finer lattice. We believe this is caused by the large distances

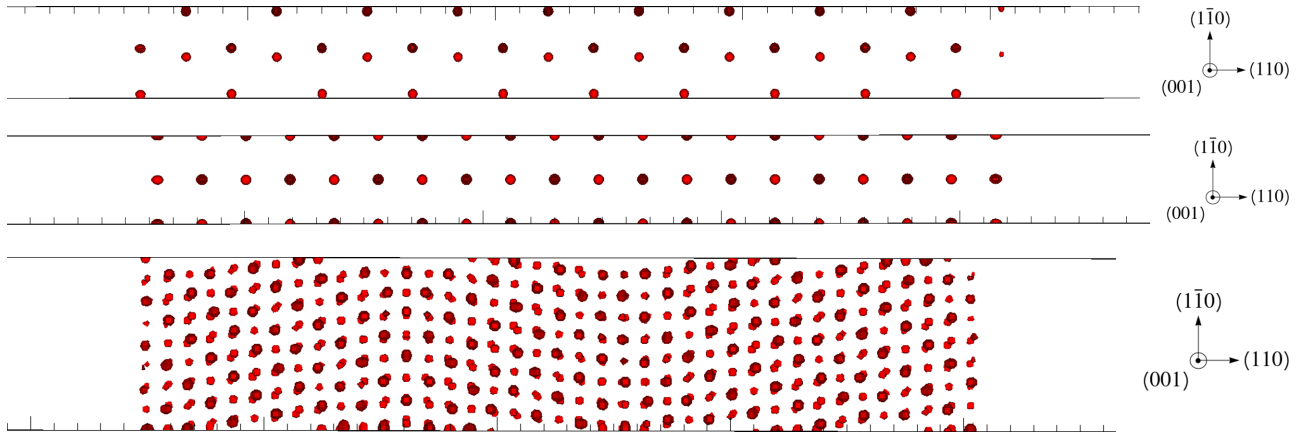


FIG. 7. BCC interface distortions in solid-vapor calculations resulting from cDFT calculations at $k_B T/\epsilon = 0.3$. The interfaces are perpendicular to the (110) direction and the (001) (i.e., z direction) is perpendicular to the image. The top figure shows the positions of atoms (density peaks) after relaxation where different shades indicate different z positions. The structure is distorted throughout the crystal, and the interfaces are not flat in contrast to the middle image in which only the densities in the four layers at the interface were allowed to relax (thus more faithfully simulating a semi-infinite bulk crystal). The lower image shows results of unconstrained relaxation with a coarser grid ($\Delta \approx 0.2\sigma$). The interior structure is distorted but the faces remain flat. These images were generated using Visit [39].

between computational grid sites, which prevents a proper relaxation along the direction normal to the interface. A better arrangement of the atomic positions is thus found by making an angle with the z axis, which allows for intermediate distances between atoms to be accessible.

The instability of the BCC structure also disappears when we increase the temperature. In Fig. 8 we show that when the temperature increases, the free energy of the minima corresponding to the shifted plane also increases and eventually disappears when the temperature reaches the vapor-liquid-

BCC triple point. This is in agreement with the observation of a stable BCC structure in the liquid-solid coexistence region, at higher temperatures.

Finally, Fig. 8 also shows results for hard spheres. In this case, there is only a single (high-density) fluid phase and there is no instability. This is consistent with the fact that no instability is seen in the LJ fluid interface since at high temperatures, the LJ system approaches the hard-sphere limit.

The conclusion is that the LJ BCC crystal-vapor interface is indeed unstable below the triple point, at least for the (110) plane. Our observations are in agreement with previous work, see, e.g., Ref. [40] and the remarks in Swope and Andersen [41]. We were nevertheless able to determine BCC surface tensions for all three planes by using a modified procedure whereby the BCC slab was taken from a previously relaxed perfect crystal and the interior of the slab was frozen (i.e., not allowed to relax), with only the layers near the interface relaxing. Further details of the procedure, and a comparison to unconstrained calculations in the case of FCC, are given in Appendix D. Finally, having identified this instability, we tested it for the case of a BCC-liquid interface and found that even when starting with a displacement in the unstable direction, the system relaxed to a perfect BCC-liquid interface thus suggesting (but not proving) that the BCC-liquid interface is metastable, as opposed to the BCC-vapor case.

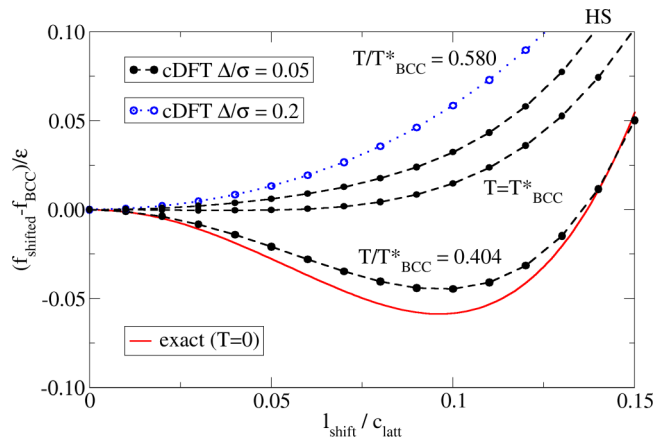


FIG. 8. Variation of the Helmholtz free energy per particle (i.e., the internal energy per particle in the case of the zero-temperature limit) as we shift the atom positions on one of the (110) planes. The red curve shows the exact zero-temperature results while the dotted and dashed lines show partially relaxed cDFT calculations for two different grid spacings. The minimization in the cDFT calculations is constrained to Gaussian peaks for the solid density, in order to keep the atoms in place. For LJ, the thermodynamic conditions are that of the BCC-vapor coexistence while for hard spheres it is BCC-fluid coexistence. The black curve labeled “HS” are results of hard-sphere calculations.

IV. CONCLUSIONS

The work presented here demonstrates that classical density functional theory can be used to determine the surface free energies for both hard spheres and the Lennard-Jones potential. For hard spheres, our results show that the explicitly stable FMT gives surface free energies that compare as well to simulation as the older White Bear models. For the LJ solid, we determined the surface tensions for the three lowest-index faces for both the FCC and BCC phases in contact with the liquid phase (the melt) and the vapor phase. It was noted that, in accord with zero-temperature results, the BCC-vapor

interface is unstable for certain crystal faces but there was no indication that this was the case for the interface with the liquid. Although our cDFT model is not expected to be quantitatively accurate, we nevertheless found that when the temperature is scaled to the triple point, the FCC surface tensions compare reasonably well to the available simulation results. Interestingly, the differences between the surface tensions of the crystal faces seems to become very small (perhaps to vanish) at the triple point—for both the vapor and the liquid—and to increase as one moves away from it.

Our methods should be applicable to a wide range of systems involving other interaction potentials. Furthermore, the results can be used to parametrize simple models for the free energy of interfacial systems such as the capillary model that is a key ingredient of classical nucleation theory [1]. In particular, we have recently discussed the use of our results to understand the competition between FCC and BCC phases during the crystallization in LJ systems [42].

ACKNOWLEDGMENTS

The work of C.S. was funded by the Belgian National Fund for Scientific Research (FRS-FNRS) under the FRIA grant FC 38825. That of J.F.L. was supported by the European Space Agency (ESA) and the Belgian Federal Science Policy Office (BELSPO) in the framework of the PRODEX Programme, Contract No. ESA AO-2004-070.

APPENDIX A: THE CDFT FUNCTIONAL

The cDFT functional used in this work is the “standard” model consisting of a hard-sphere contribution and a mean-field treatment of the attractive part of the potential,

$$F[\rho] = F_{\text{HS}}(d(T; [v_0]), T; [\rho]) + \frac{1}{2} \int d\mathbf{r}_1 \int d\mathbf{r}_2 \rho(\mathbf{r}_1) \rho(\mathbf{r}_2) w_{\text{att}}(r_{12}). \quad (\text{A1})$$

The potential is divided in two using the standard WCA prescription [45–47] $v(r) = v_0(r) + w(r)$ with the short-ranged part,

$$v_0(r) = [v(r) - v(r_0)] \Theta(r_0 - r), \quad (\text{A2})$$

where r_0 is the minimum of the potential $v(r)$ and $\Theta(x)$ is the step function which has value one for $x > 0$ and zero for $x < 0$. The attractive part of the potential is $w(r) = v(r) - v_0(r)$. From this, we calculate the effective hard-sphere diameter using the Barker-Henderson prescription [48],

$$d = \int_0^{r_0} (1 - e^{-\beta v_0(r)}) dr. \quad (\text{A3})$$

The hard-sphere part is divided into an ideal-gas contribution and an excess contribution,

$$F_{\text{HS}}(d, T; [\rho]) = F_{\text{ideal}}(T; [\rho]) + F_{\text{ex}}(d, T; [\rho]), \quad (\text{A4})$$

where the (exactly known) ideal gas functional is

$$F_{\text{ideal}}(T; [\rho]) = k_B T \int [\rho(\mathbf{r}) \ln \rho(\mathbf{r}) - \rho(\mathbf{r})] d\mathbf{r}. \quad (\text{A5})$$

For the excess part we use the fundamental measure form

$$F_{\text{ex}}(d, T; [\rho]) = \int \Phi[\bar{n}(\mathbf{r}, d; [\rho])] d\mathbf{r}, \quad (\text{A6})$$

where $\Phi(\bar{n})$ is a rational function of the *fundamental measures*, $\bar{n}(\mathbf{r}, d; [\rho])$, which are linear convolutions of the local density:

$$n_\alpha(\mathbf{r}, d; [\rho]) = \int w_\alpha(\mathbf{r} - \mathbf{r}'; d) \rho(\mathbf{r}') d\mathbf{r}'. \quad (\text{A7})$$

The weights used in FMT (for a single species) are $w_\eta(\mathbf{r}, d) = \Theta[(d/2) - |\mathbf{r}|]$, which generates the average of the density over a the volume of a hard-sphere, and the scale, vector, and tensor weights $w_s(\mathbf{r}, d) = \delta[(d/2) - |\mathbf{r}|]$, $\mathbf{w}_v(\mathbf{r}, d) = \hat{\mathbf{r}}\delta[(d/2) - |\mathbf{r}|]$ and $\mathbf{w}_T(\mathbf{r}, d) = \hat{\mathbf{r}}\hat{\mathbf{r}}\delta[(d/2) - |\mathbf{r}|]$ respectively, which average the density over a sphere of diameter d . Different versions of FMT (e.g., “White Bear,” “esFMT,” etc.) are distinguished by their particular forms for the function Φ . We use the “explicitly stable FMT” or esFMT introduced in Ref. [21] for which

$$\Phi(\bar{n}) = -\frac{1}{\pi d^2} n_s \ln(1 - n_\eta) + \frac{1}{2\pi d} \frac{n_s^2 - n_v^2}{1 - n_\eta} + \frac{1}{24\pi} \times \frac{n_s^3 - 3n_s n_v^2 + 3\mathbf{n}_v \cdot \mathbf{n}_T - \text{Tr}(\mathbf{n}_T^3)}{(1 - n_\eta)^2}. \quad (\text{A8})$$

APPENDIX B: DETERMINATION OF THE INTERFACIAL FREE ENERGY

1. Computational grid

The calculations are performed on a $N_x \times N_y \times N_z$ computational grid with spacings Δ_x , Δ_y , and Δ_z . The dimensions of the computational grid are chosen to match multiples of the solid lattice constants by adjusting the grid spacings. The number of points N_x , N_y , N_z are fixed and are multiples of the points N'_x , N'_y , N'_z defining a single solid cell. It is important to keep the same number of points for the grid—up to an integer multiple—in order to be consistent with the thermodynamics of the discrete system (physical properties such as the bulk free energies at coexistence will depend on the discretization). We find that working with the same number of points across calculations is easier than imposing a fixed spacing, because we can determine the equilibrium lattice constants with continuous increments in the grid spacing, rather than by discrete jumps as we would have by changing the number of points. Finally, the lattice constants used in the interface calculations are determined from homogeneous (bulk) calculations and correspond to those of the relaxed solid at coexistence with the fluid phase.

To compute the interfacial free energies for multiple planes of the BCC and FCC lattices, we have to orient the solid in the (rectangular) computational grid so as to expose the desired Miller plane on one of the slab. The common representation of the BCC and FCC lattices already features the (001) plane on the side of the cubic cell; the task is, however, nontrivial for all other cases. The bases we used are given in Table II for all lattices and planes considered. The relative dimensions of the rectangular cells as well as the exact number of points N'_x , N'_y , N'_z that constitute each unit cell are given in Table III.

TABLE II. Bases of the rectangular cells used to describe the BCC and FCC solid lattices, depending on the Miller plane that must be exposed on the side (looking from the z direction).

BCC (001)			BCC (110)			BCC (111)			FCC (001)			FCC (110)			FCC (111)		
0	0	0	0	0	0	1/6	1/2	0	0	0	0	0	0	0	0	0	0
1/2	1/2	1/2	1/2	1/2	0	0	0	1/3	1/2	1/2	0	1/2	1/2	1/2	1/2	1/2	0
			1/2	0	1/2	1/6	1/2	1/2	1/2	0	1/2				1/2	1/6	1/3
			0	1/2	1/2	0	0	5/6	0	1/2	1/2				0	2/3	1/3
						1/2	1/2	1/3							0	1/3	2/3
						1/3	0	2/3							1/2	5/6	2/3
						1/2	1/2	5/6									
						1/3	0	1/6									
						5/6	1/2	2/3									
						2/3	0	0									
						5/6	1/2	1/6									
						2/3	0	1/2									

The numbers N'_x, N'_y, N'_z are chosen in a way that the grid spacings are as close as possible to a target value, usually $\Delta \equiv \Delta_x = \Delta_y = \Delta_z = 0.05\sigma$, considering the usual dimensions of the unit cell. Out of convenience, we keep the same values across all calculations (the lattice constants do not change drastically between different thermodynamic conditions). We also made some calculations with the larger spacings $\Delta \approx 0.2\sigma$ using the same number of points N'_x, N'_y, N'_z that we used for the fine grid $\Delta \approx 0.05\sigma$, and we simply used four times more unit cells in the computational grid. This way the number of points is still large enough to remain close to the target spacing, in this case $\Delta = 0.2\sigma$.

2. Thermodynamic parameters

The thermodynamic parameters as calculated for a computational grid with spacing $\Delta/\sigma = 0.05$ are given in Table IV.

3. Initial condition

The solid phase is initialized using Gaussian peaks located at the lattice positions, and occupies about half of the computational grid. The peaks are normalized to $1 - c$, where $c > 0$ is a vacancy concentration usually set to 0.01. Addition of the liquid requires some care due to the fact that all FMT free energy functionals diverge when the local packing fraction, the fundamental measure $n_\eta(\mathbf{r})$, is greater to or equal to one. In the solid, particularly the FCC phase, at low temperatures, the local packing fraction is very close to this threshold near

the lattice sites, so that simply adding the uniform fluid can easily lead to divergent profiles. We have used two different methods, depending on the particular interface. In the first method we start with a sharp interface between the fluid and solid phases, leaving a gap of one hard-sphere diameter in length to separate the Gaussian peaks from the homogeneous fluid density $\rho_f(\mathbf{r})$:

$$\rho(\mathbf{r}) = \begin{cases} \rho_s(\mathbf{r}) & \text{if } |z| < L_z/4 \\ 0 & \text{if } L_z/4 < |z| < L_z/4 + \sigma \\ \rho_f(\mathbf{r}) & \text{if } L_z/4 + \sigma < |z| < L_z/2 \end{cases}, \quad (\text{B1})$$

where $\rho_s(\mathbf{r})$ is the sum of the Gaussian peaks approximating the solid density. To compensate for the presence of the gap, we initialized the fluid density with the coexistence value multiplied by the ratio V_f/V'_f of volumes of the fluid region with and without the gap.

The second method is a smooth interpolation between the Gaussian peaks and the homogeneous fluid density,

$$\rho(\mathbf{r}) = \rho_s(\mathbf{r})f(z; z_1, w) + \rho_f(\mathbf{r})f(z; z_2, w), \quad (\text{B2})$$

using two double sigmoid functions,

$$f(z; z_0, w) = \frac{1}{2} \left[\tanh\left(\frac{z_0 + z}{w}\right) + \tanh\left(\frac{z_0 - z}{w}\right) \right]. \quad (\text{B3})$$

The inflection points of the double sigmoids, z_1 and $z_2 = z_1 + \sigma$, are located one hard-sphere diameter apart, once again to avoid nonphysical packing fractions. The parameters are set

 TABLE III. Dimensions of the rectangular cells in terms of the interatomic distance d . Columns 2–4 give the lattice constants for the solid lattice. Columns 5–7 give the number of points used for the computational grid in most calculations. The last two columns give the number of planes, per unit cell, normal to the z direction as well as the interplanar distances d_{planes} .

Lattice (plane)	a_{latt}/d	b_{latt}/d	c_{latt}/d	N'_x	N'_y	N'_z	No. planes	d_{planes}/d
BCC (001)	$2/\sqrt{3}$	$2/\sqrt{3}$	$2/\sqrt{3}$	26	26	26	2	$1/\sqrt{3}$
BCC (110)	$2/\sqrt{3}$	$\sqrt{8/3}$	$\sqrt{8/3}$	26	37	37	2	$\sqrt{2/3}$
BCC (111)	$2\sqrt{2}$	$\sqrt{8/3}$	2	64	37	45	6	1/3
FCC (001)	$\sqrt{2}$	$\sqrt{2}$	$\sqrt{2}$	32	32	32	2	$1/\sqrt{2}$
FCC (110)	$\sqrt{2}$	1	1	32	23	23	2	1/2
FCC (111)	1	$\sqrt{3}$	$\sqrt{6}$	23	40	56	3	$\sqrt{2/3}$

TABLE IV. Lennard-Jones critical point and triple points in the cDFT model.

	kT/ϵ	$\rho_{\text{vapor}}\sigma^3$	$\rho_{\text{liquid}}\sigma^3$	$\rho_{\text{solid}}\sigma^3$
Liq-Vap critical point	1.295	0.245	0.245	–
FCC triple point	0.798	9.83×10^{-3}	0.675	0.916
BCC triple point	0.742	6.12×10^{-3}	0.704	0.874

to $z_1 = L_z/4$ and $w = \sigma/2$ for vapor-solid interfaces and $w = 2\sigma$ for the liquid-solid case, where the interface is wider.

The liquid-solid data shown in the main text have been generated using the first initialization method. In the vapor-solid case, the first method has been used for the FCC (001), FCC (111), and BCC (001) curves, but not for the three others. FCC (110) has been initialized with the smooth interface and due to the BCC instability, BCC (110) and (111) have been generated with a different protocol, described in Sec. D. In that case, the initial condition used the same formula (B2) to create a smooth interface but the solid density is not a sum of Gaussian peak but rather the fully relaxed profile at coexistence. In the end, we find that both methods lead to the same results and the exact shape of the initial profile is not very important. The use of two different initialization methods was simply a result of experimentation to see if one method might lead to faster convergence than another but in the end no such trend was found.

4. Minimization of the density functional

The functional is minimized using a modified version of the FIRE2 algorithm, a kind of gradient descent with inertia described in [27]. In the low-temperature interface calculations, the free energy landscape is very hard to navigate through because, as mentioned above, the local packing fractions are very close to one in the fully relaxed solid. This means the minimization algorithms can end up wasting significant time stepping into the unphysical region and backtracking. To avoid this, we added an additional term to the FMT functional that creates an artificial cost for stepping close to $\eta = 1$. The new functional,

$$F_\lambda[\rho] = F[\rho] + \int \frac{\lambda}{(1 - \eta(\mathbf{r}))^2} d\mathbf{r}, \quad (\text{B4})$$

is used to iterate minimizations starting with a large amplitude for the repulsive term and then progressively decrease it until no significant change in the physical properties can be detected. We usually chose to reduce λ by a factor of 10 each step, starting from $\beta\lambda\sigma^3 = 10^{-7}$ and going down to $\beta\lambda\sigma^3 = 10^{-17}$. The typical relative difference between the last two iterations is around 10^{-5} for the interfacial free energy. The effect of this mechanism is to allow the densities in regions away from the lattice peaks to relax before making the fine adjustments needed at the peaks.

5. Minimizing at constant chemical potential and minimizing at constant particle number is equivalent

The two calculations discussed in the main text were minimizing the functional $\Lambda_\mu[\rho] = F[\rho] - \mu N[\rho]$ at fixed

chemical potential, μ , and minimizing the Helmholtz functional $F[\rho]$ at constant particle number, N_0 . The latter can be implemented by introducing a Lagrange parameter to define

$$L_{N_0}[\rho] = F[\rho] - \lambda(N[\rho] - N_0) \quad (\text{B5})$$

and minimizing to get

$$0 = \frac{\delta L_{N_0}[\rho]}{\delta \rho(\mathbf{r})} = \frac{\delta F[\rho]}{\delta \rho(\mathbf{r})} - \lambda, \\ 0 = \frac{\partial L_{N_0}[\rho]}{\partial \lambda} = N[\rho] - N_0. \quad (\text{B6})$$

Multiplying the former by the density, integrating and making use of the latter gives

$$\lambda = \frac{1}{N_0} \int \rho(\mathbf{r}) \frac{\delta F[\rho]}{\delta \rho(\mathbf{r})} d\mathbf{r} \quad (\text{B7})$$

so that the calculation reduces to

$$\frac{\delta F[\rho]}{\delta \rho(\mathbf{r})} = \frac{1}{N_0} \int \rho(\mathbf{r}) \frac{\delta F[\rho]}{\delta \rho(\mathbf{r})} d\mathbf{r}. \quad (\text{B8})$$

In contrast, minimization at constant chemical potential gives

$$\frac{\delta F[\rho]}{\delta \rho(\mathbf{r})} = \mu, \quad (\text{B9})$$

so that it is clear that minimizing at constant particle number N_0 to get the density $\rho_{N_0}(\mathbf{r})$ gives the same result as minimizing at constant chemical potential

$$\mu = \frac{1}{N_0} \int \rho_{N_0}(\mathbf{r}) \frac{\delta F[\rho]}{\delta \rho_{N_0}(\mathbf{r})} d\mathbf{r}, \quad (\text{B10})$$

and the two procedures are therefore equivalent.

Another way to look at this is to introduce the parameterization

$$\rho_N(\mathbf{r}; [g]) = N \frac{g(\mathbf{r})}{\int g(\mathbf{r}') d\mathbf{r}'}, \quad (\text{B11})$$

in which case the usual grand-canonical minimization of $\Omega[\rho]$ with respect to density now becomes minimization of $\Omega[\rho_N[g]]$ with respect to both N and $g(\mathbf{r})$. Holding N constant and minimizing only with respect to g gives

$$0 = \frac{\delta \Omega[\rho_N[g]]}{\delta g(\mathbf{r})} = \int \left(\frac{\delta \Omega[\rho]}{\delta \rho(\mathbf{r}')} \right)_{\rho=\rho_N[g]} \frac{\delta \rho_N(\mathbf{r}'; [g])}{\delta g(\mathbf{r})} d\mathbf{r}', \quad (\text{B12})$$

and using

$$\frac{\delta \Omega[\rho]}{\delta \rho(\mathbf{r}')} = \frac{\delta F[\rho]}{\delta \rho(\mathbf{r}')} - \mu, \\ \frac{\delta \rho_N(\mathbf{r}'; [g])}{\delta g(\mathbf{r})} = [\delta(\mathbf{r}' - \mathbf{r}) - 1] \frac{N}{\int g(\mathbf{r}'') d\mathbf{r}''} \quad (\text{B13})$$

gives

$$\left(\frac{\delta F[\rho]}{\delta \rho(\mathbf{r})} \right)_{\rho=\rho_N[g]} = \frac{1}{N} \int \rho_N(\mathbf{r}; [g]) \left(\frac{\delta F[\rho]}{\delta \rho(\mathbf{r})} \right)_{\rho=\rho_N[g]} d\mathbf{r}, \quad (\text{B14})$$

which is the same as Eq. (B8) except that now we solve for g . In the following, we will denote the chemical potential

resulting from this minimization with respect to g at constant N as

$$\mu_N \equiv \frac{1}{N} \int \rho_N(\mathbf{r}; [g]) \left(\frac{\delta F[\rho]}{\delta \rho(\mathbf{r})} \right)_{\rho=\rho_N[g]} d\mathbf{r}. \quad (\text{B15})$$

6. Protocol for determining the surface tension and resulting finite-size effects

a. The protocol

Minimizing the free energy for an interfacial system at constant chemical potential can only be done at phase coexistence. This means that one must know the chemical potential for coexistence exactly: any error will lead to the interface moving until one phase fills the entire computational cell. Furthermore, for a finite system, the chemical potential that gives phase coexistence will not be the same as that for bulk coexistence because the effects of the interface extend into the “bulk” region so that, in principle, one has to move infinitely far from the interface in order for the density to reach its bulk value.

On the other hand, minimizing at constant particle number always gives phase coexistence with different values of the total number of particles being accommodated by changing the size of the two “bulk” regions, with no change to the interface. When one of the phases is a solid, however, there are additional complications. In the extreme case of a solid-vapor interface, the interface cannot be moved continuously since it involves discrete lattice planes for the solid. So, starting with a complete planar interface and adding some mass, the mass must partly go into creating a new partial crystal plane and partly into raising the density of the vapor. The former will inevitably increase the interfacial energy and the latter increases the chemical potential. One therefore expects that, starting with a complete crystal plane, as mass is added the surface tension will increase, reach some maximum and then decrease again until reaching a minimum when a new crystal plane is formed with a corresponding variation of the chemical potential. This is illustrated in Fig. 2, taken from our calculations.

Our protocol for determining the surface tension is therefore as follows. First, an interfacial system is equilibrated at constant particle number, N , giving in the end the relaxed density, $\rho_N(\mathbf{r})$, and the chemical potential μ_N as defined above. We then determine the bulk properties of the two phases at this chemical potential by minimizing the grand-canonical free energy giving the average bulk density of each phase, $\bar{\rho}_{\mu_N,i}$, as well as its grand-potential free energy density $\omega_{\mu_N,i}$ and the corresponding Helmholtz free energy densities $f_{N,i} = \omega_{\mu_N,i} - \mu_N \bar{\rho}_{\mu_N,i}$. The Gibb's partition is determined using $V_{N,1} + V_{N,2} = V$ and $V_{N,1} \bar{\rho}_{N,1} + V_{N,2} \bar{\rho}_{N,2} = N$ giving $V_{N,1} = \frac{N - \bar{\rho}_{N,2} V}{\bar{\rho}_{N,1} - \bar{\rho}_{N,2}}$, etc., and the excess surface free energy calculated as

$$\begin{aligned} \gamma_N &= \frac{\Omega_\mu[\rho_N] - \omega_{\mu_N,1} V_{N,1} - \omega_{\mu_N,2} V_{N,2}}{2A} \\ &= \frac{F[\rho_N] - f_{N,1} V_{N,1} - f_{N,2} V_{N,2}}{2A}, \end{aligned} \quad (\text{B16})$$

where A is the area of the planar interface. As argued above, the finite-size effects mean that the chemical potential is not

that at bulk coexistence which, in turn, implies that in general $\omega_{\mu_N,1} \neq \omega_{\mu_N,2}$.

b. N dependence for a finite system

We examine the N dependence of the surface tension by calculating the derivative

$$\begin{aligned} 2A \frac{d\gamma_N}{dN} &= \int \left(\frac{\delta \Omega[\rho]}{\delta \rho(\mathbf{r}')} \right)_{\rho_N} \frac{d\rho_N(\mathbf{r}')}{dN} d\mathbf{r}' - \frac{d\omega_{\mu_N,1}}{dN} V_1 \\ &\quad - \frac{d\omega_{\mu_N,2}}{dN} V_2 - \omega_{\mu_N,1} \frac{dV_1}{dN} - \omega_{\mu_N,2} \frac{dV_2}{dN}. \end{aligned} \quad (\text{B17})$$

Using Eq. (B8), one has that

$$\begin{aligned} \frac{d\Omega[\rho_N]}{dN} &= \int \left(\frac{\delta F[\rho]}{\delta \rho(\mathbf{r}')} \right)_{\rho_N} \frac{d\rho_N(\mathbf{r}')}{dN} d\mathbf{r}' - \frac{d\mu_N N}{dN} \\ &= \mu_N \int \frac{d\rho_N(\mathbf{r}')}{dN} d\mathbf{r}' - N \frac{d\mu_N}{dN} - \mu_N \\ &= -N \frac{d\mu_N}{dN}, \end{aligned} \quad (\text{B18})$$

and similarly for the homogeneous contributions, assuming that the homogeneous calculations are performed in a volume of size V_0 ,

$$\begin{aligned} \frac{d\omega_{\mu_N,i}}{dN} &= \frac{1}{V_0} \frac{d\Omega_{\mu_N,i}}{dN} \\ &= \frac{1}{V_0} \frac{d[F[\rho_{\mu_N,i}] - \mu_N \int \rho_{\mu_N,i}(\mathbf{r}) d\mathbf{r}]}{dN} \\ &= \frac{1}{V_0} \int \left(\frac{\delta F[\rho]}{\delta \rho(\mathbf{r}')} \right)_{\rho_{\mu_N,i}} \frac{d\rho_{\mu_N,i}(\mathbf{r}')}{dN} d\mathbf{r}' \\ &\quad - \frac{1}{V_0} \frac{d[\mu_N \int \rho_{\mu_N,i}(\mathbf{r}) d\mathbf{r}]}{dN} \\ &= -\bar{\rho}_{\mu_N,i} \frac{d\mu_N}{dN}, \end{aligned} \quad (\text{B19})$$

giving the exact result

$$2A \frac{d\gamma_N}{dN} = -\frac{\omega_{\mu_N,1} - \omega_{\mu_N,2}}{\bar{\rho}_{\mu_N,1} - \bar{\rho}_{\mu_N,2}}. \quad (\text{B20})$$

Let the value of the chemical potential and free energy density at bulk coexistence be μ_{12}^* and ω_{12}^* , respectively. For a liquid-vapor interface, one expects the differences between $\omega_{\mu_N,i}$ and μ_N and the bulk coexistence quantities to be small and decreasing with system size so $d\gamma_N/dN$ should be similarly small and decreasing with system size. On the other hand, for a solid-vapor interface, as explained above, one expects the surface tension to go through a periodic variation as mass is added and new crystal planes are formed. This implies that during each cycle, $d\gamma_N/dN$ should go to zero twice: at the minimum and the maximum of the surface tension so that in both cases, one must have $\omega_{\mu_N,1} = \omega_{\mu_N,2}$. Since this is also expected to hold at bulk coexistence and since one expects the thermodynamic limit to correspond to the case of perfectly formed crystal planes, the minimum value of the surface tension, as a function of N , would seem to be the best estimate.

c. Reducing the computational effort

It is possible to reduce the need for determining the bulk free energies for every value of N as is needed in Eq. (B16). To derive the expression, let the index a stand for either phase 1 or phase 2 and b be the other. Then expanding about the bulk coexistence values gives

$$f_{N,a} \approx f_a^* + f_a'^*(\rho_{\mu_N,a} - \rho_a^*) = f_a^* + \mu^*(\rho_{\mu_N,a} - \rho_a^*) \quad (\text{B21})$$

and

$$V_{N,a} \approx V_{N,a}^* - \frac{V_{N,a}^*}{\rho_a^* - \rho_b^*}(\rho_{\mu_N,a} - \rho_a^*) - \frac{V_{N,b}^*}{\rho_a^* - \rho_b^*}(\rho_{\mu_N,b} - \rho_b^*) \quad (\text{B22})$$

so that

$$f_{N,a}V_{N,a} \approx f_a^*V_a^* + \mu^*(\rho_{\mu_N,a} - \rho_a^*)V_{N,a}^* - f_a^* \frac{V_{N,a}^*}{\rho_a^* - \rho_b^*}(\rho_{\mu_N,a} - \rho_a^*) + f_a^* \frac{V_{N,b}^*}{\rho_a^* - \rho_b^*}(\rho_{\mu_N,b} - \rho_b^*). \quad (\text{B23})$$

Adding the contributions for the two phases and simplifying gives

$$f_{N,1}V_{N,1} + f_{N,2}V_{N,2} \approx f_1^*V_1^* + f_2^*V_2^* + [\mu^*(\rho_1^* - \rho_2^*) - (f_1^* - f_2^*)] \times \frac{V_{N,1}^*(\rho_{\mu_N,1} - \rho_1^*) + V_{N,2}^*(\rho_{\mu_N,2} - \rho_2^*)}{\rho_1^* - \rho_2^*}. \quad (\text{B24})$$

However, the combination $\mu\rho - f = p$, the pressure, and at coexistence $p_1^* = p_2^*$ so the term involving the chemical potential vanishes showing that, up to second order, one has that

$$\gamma_N \approx \frac{F[\rho_{\mu_N}] - f_1^*V_{N,1}^* - f_2^*V_{N,2}^*}{2A}, \quad (\text{B25})$$

which is the expression used in our calculations.

7. Bulk free energies

The bulk phases are homogeneous because they possess translational symmetry: continuous translational symmetry in the fluid phases (i.e., the density is a constant independent of position) or discrete translational symmetry in the solid (determined by the Bravais lattice). In the case of the fluid, the determination of the density therefore reduces to solving an algebraic equation. For the solid one must perform a full, three-dimensional cDFT minimization. For this, the density was initialized with Gaussian peaks centered on the lattice positions, which are normalized to $1 - c$, where $c > 0$ is the vacancy concentration in the solid. We chose to minimize the density functional at constant particle number because it was found to be more convenient to have direct control over the vacancy concentration. So, the minimizations were performed for several concentrations of vacancies starting from 1×10^{-2} and dividing by 2 until reaching 1×10^{-6} . The solid properties over this range of densities, including effective chemical potentials and the free energies, are returned as an output of

TABLE V. Interfacial free energies from zero-temperature calculations. The quantity shown is $\gamma\sigma^2/\varepsilon$ for different levels of relaxation: nothing relaxed, relaxing the distances between solid planes parallel to the interface, and relaxing all the atom positions.

Interface type	Not relaxed	Relaxing planes	Relaxing atoms
FCC (001)	2.604	2.585	2.578
FCC (110)	2.752	2.737	2.739
FCC (111)	2.485	2.480	2.474
BCC (001)	2.508	2.438	2.431
BCC (110)	2.379	2.373	–
BCC (111)	2.692	2.680	–

the calculation. We then use interpolations of these properties to minimize the free energy with respect to lattice constant and vacancy concentration at constant chemical potential.

Because our implementation does not allow precise calculations below $c \approx 10^{-6}$, we extrapolate the solid free energies at higher chemical potentials assuming that the Helmholtz free energy per unit volume and density does not vary for such small changes in the vacancy concentration. This extrapolation step is necessary to compute the solid bulk properties at low temperatures since the vacancy concentrations are extremely small.

APPENDIX C: ZERO-TEMPERATURE CALCULATIONS

1. Surface free energies

Exact calculations can be carried out for a vacuum-solid interface at a temperature of absolute zero. This is a limit case for the vapor-solid calculations since the vapor density goes to zero with the temperature. The interfacial free energy is computed by summing the inter-particle energies of all pair of atoms, $U = \frac{1}{2} \sum_{i \neq j} v(r_{ij})$, for a solid lattice in a rectangular box with periodic boundary conditions only in the x and y directions. The periodicity is purposefully broken in the z direction in order to mimic the presence of an interface with a vacuum.

The computational grid is made out of $1 \times 1 \times N$ unit cells of the solid, using the same bases and dimensions given in Tables II and III. When computing the total energy of the solid slab, we make enough copies of the lattice in the x and y directions in order to compute all the interactions up to the potential cutoff distance. The number of cells in the z direction, N , is large enough so that the two interfaces do not interact with each other. In practice, the length of the computational cells in the z direction are so that there are at least 25 solid planes in the slab.

The dimensions of the computational grid are that of the relaxed solid cell at coexistence with the vacuum. The corresponding lattice constants are found by minimizing the internal free energy of a homogeneous solid (i.e., with periodic boundary conditions in all directions). The lengths in the x and y directions are fixed during the relaxation but the length in the z direction is allowed to change so that the interplanar distances can relax.

In Table V we give three sets of data for the surface free energies. The first set are interfacial free energies computed

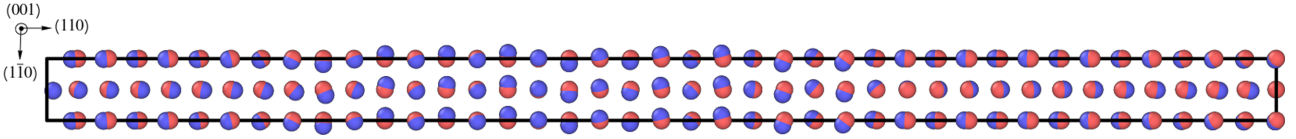


FIG. 9. Instability of the BCC interface in a zero-temperature calculation: Relaxed atoms (in blue) starting from the regular BCC lattice positions (in red). The displacements of the atoms in the slab are the same as those shown in Fig. 10 (same projection on the first image). These displacements are almost parallel to (110) planes, but due to random perturbations imposed on the initial lattice the system is divided in domains where the shift of the atomic positions occurred in different directions. The side lengths of the box in the directions parallel to the interface are kept fixed during the minimization of the internal energy and have periodic boundary conditions. The direction normal to the interface does not have periodic boundary conditions to emulate the presence of an interface with a vacuum, located on the left and right faces of the box. The length in the normal direction is allowed to change, but this image shows a superposition of the initial and final configurations where the atom positions have been rescaled to fit in the same bounding box. The initial density of the solid in the slab is the coexistence value of $1.0536 \sigma^{-3}$. The lattice dimensions have been determined using the two-atom BCC cell (not subject to the plane shift), minimizing the internal energy per particle. The visualization is performed using the program Ovito [49].

from the unrelaxed solid slab in contact with a vacuum. The surface free energy is computed in a manner similar to what we use for cDFT calculations,

$$\gamma = \frac{U_{\text{slab}} - e_{\text{hom}} N_{\text{slab}}}{2A}, \quad (\text{C1})$$

where U_{slab} is the total energy of the solid slab (no periodic boundaries in the z direction), e_{hom} is the internal energy per particle of the homogeneous solid, N_{slab} is the number of atoms in the slab and A is the contact area between the vacuum and one side of the solid slab. Note that at zero temperature, internal energies and free energies are the same quantities. In the column labeled “relaxing planes,” the interfacial free energy is given when we allow the interplanar distances to change, for planes parallel to the interface, keeping the atoms fixed on these planes. In the last column, “relaxing atoms,” all the atomic positions are allowed to change as independent variables. The results in these last two calculations are almost the same because the atoms keep the same configuration after the complete minimization. The only exception are the BCC (110) and (111) interfaces, which are subject to the (110) plane sliding instability of the BCC structure (see Fig. 9).

2. Instability of the BCC lattice

As mentioned in the main text, the BCC structure is unstable with respect to a displacement of some (110) planes. Relaxing every atom positions in our BCC (110) and (111) interface calculations result in a different structure than the regular BCC lattice, both at the interface and deep into the bulk (see Figs. 7 and 9).

We further investigate this phenomenon with zero-temperature calculations, starting from a unit cell that exposes the BCC (110) plane (see Tables II and III). We first equilibrate the cell by minimizing the internal free energy with respect to the interatomic distance. Then we slide one of the (110) planes by moving the $z = c_{\text{latt}}/2$ atoms in the y direction. Figure 8 shows the energy as a function of the displacement of the (110) plane. At zero temperature, the internal energy decreases monotonically with the displacement until an equilibrium value is reached. That equilibrium shift is $l_{\text{shift}} = 0.0963 c_{\text{latt}}$, which is $0.1572 d$ in terms of the interatomic distance. The corresponding variation for the in-

ternal energy per particle is -0.0586ϵ . Calculations in which we relax the positions of all the atoms in the cell give the same values at the level of precision considered (keeping the dimensions of the cell fixed). Figure 10 shows the resulting configuration when all the atomic positions are relaxed. In the first of the four images, the main distortion is that the middle row of atoms moves horizontally which is the sliding of the (110) plane while some smaller relaxation occurs in the two rows adjacent to the sliding row.

In addition to relaxing the atom positions, one can also relax the lattice dimensions by allowing the lattice vectors to relax. This is not a situation we encounter in our cDFT calculations, as the dimensions are fixed, but it helps understand which structure the BCC lattice is relaxing towards. What we observe by doing such calculations is that the complete relaxation of the BCC lattice end up with the HCP configuration. To show this, we once again minimized the internal energy of the homogeneous BCC solid, starting once again with the BCC (110) cell and periodic boundary conditions. In addition to the $3N$ coordinates of the atoms in the cell, six parameters are necessary to define the lattice vectors. These parameters are the three lattice constants, i.e., the vector lengths, and the three angles between them (α, β, γ). Relaxing all $3N + 6$ parameters results in an HCP configuration.

APPENDIX D: STABILIZATION BY FREEZING THE SOLID BULK

To avoid the distortions in BCC-vapor calculations, we tested a few techniques to artificially stabilize the density profile. The most practical method we found is to “freeze”

TABLE VI. Triple point temperatures T^* for various lattices and discretization spacing. The last row shows a quadratic extrapolation of the results from the three finest grid spacings.

Δ/σ	T_{BCC}^*	T_{FCC}^*
0.2	0.517	0.549
0.1	0.695	0.726
0.05	0.742	0.798
0.025	0.754	0.818
Extrap.	0.759	0.827

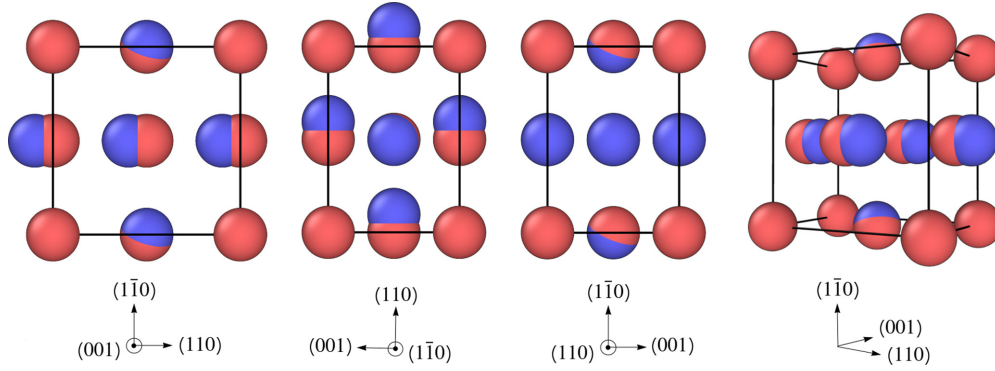


FIG. 10. Instability of the BCC lattice in a zero-temperature calculation: Relaxed atoms (in blue) starting from the lattice positions in the BCC (110) cell (in red). The lattice dimensions are kept fixed during the minimization of the internal energy. The images on the left are projections on each axis, exposing the (001), (110), and $(1\bar{1}0)$ planes, respectively. The atoms displacement are almost parallel to the (110) plane. In this example the density of the solid is $1.0536 \sigma^{-3}$, as in Fig. 9. The visualization is performed using the program Ovito [49].

the bulk solid by preventing the density profile from being relaxed in a large portion of the solid slab. We do this by setting the free energy derivatives to zero in this region so that the densities are never updated in the minimization algorithm. (Note that in this case, the bulk region is initialized with fully relaxed densities coming from a homogeneous-solid calculation.)

The FCC (001) solid-vapor interface, which is stable under all circumstances, was used as a test case to quantify the amount by which we overestimate interfacial free energies calculated using this method. Allowing the density to relax in a region of about 5σ deep in the solid slab, which is about the width of the interface, we found that the interfacial free energy is $3 \times 10^{-3} \varepsilon/\sigma^2$ higher than the value from unconstrained calculations.

APPENDIX E: ESTIMATION OF UNCERTAINTIES

Uncertainties on the surface free energies are introduced in many steps of the calculations, due to limits on computational resources. In this Appendix we list the major sources of errors and estimate their contribution to the overall uncertainty.

The first major source of error is the finite size of the computational cell. This is already the cause of the non-monotonic variation of the free energy, which is detailed in Appendix B 6 b. Another effect to consider is that if the solid slab is too small the two interfaces can interact with each other and this will corrupt the value for the surface free energy. We

TABLE VII. Influence of the discretization spacing on the properties of the FCC (001) interface computed at $kT/\varepsilon = 0.1$. The interfacial free energies in different reduced units are shown next to each other for comparison. Triple point values are marked with an asterisk.

Δ/σ	$\gamma\sigma^2/\varepsilon$	$\gamma^*\sigma^2/\varepsilon$	T/T^*
0.2	2.15	1.17	0.182
0.1	2.33	0.92	0.138
0.05	2.38	0.90	0.125
0.025	2.46	0.91	0.122

checked liquid-solid calculations by comparing two sets of results: the first generated with cells about 50σ in length and the second with larger cells of about 80σ . The values in both sets are very similar, the difference lying between 10^{-4} and $10^{-3} \varepsilon/\sigma^2$. Only the FCC (111) and BCC (110) calculations show a greater dependence on the system size with differences in free energies as large as $0.02 \varepsilon/\sigma^2$. For vapor-solid calculations, we simply compared the values of the reported surface free energy minima and that after the removal of one lattice plane. Since the interfaces are sharper at low temperatures, we consider that this is a good estimation for the magnitude of the interaction between the two interfaces. The differences are once again smaller than $10^{-3} \varepsilon/\sigma^2$.

Another source of error is the finite size of the discretization spacing. Tables VI and VII show the effect of the discretization on triple point temperatures and on the FCC (001) surface free energy at a low temperature, respectively. The last table shows a difference of about $0.08 \varepsilon/\sigma^2$ between surface free energies calculated using the finest spacings we could afford. Table I also shows a few surface free energies for different spacings, in the case of a hard-sphere interface, showing a smaller variation of about $0.02 \varepsilon/\sigma^2$. Although the influence of the discretization spacing can be quite large, it is not so important to us since we compare systems defined on computational grids with very similar values for the discretization spacing. Therefore, we do *not* consider that

TABLE VIII. Influence of small variations in the lattice spacing Δ as we change the number of points $N' \equiv N_x = N_y = N_z/N_{\text{cells}}$ in the computational cell. The solid in these calculations is FCC, and the interface exposes the (001) plane. The dimensions of the computational grid are that of $1 \times 1 \times N_{\text{cells}}$ solid units cells. These numbers can be used to estimate the inaccuracies in comparisons of data from slightly different spacings.

Type	kT/ε	N'	N_{cells}	Δ/σ	a_{latt}/σ	$\gamma\sigma^2/\varepsilon$
Vapor-solid	0.1	32	30	0.0490	1.5674	2.384
Vapor-solid	0.1	33	30	0.0476	1.5694	2.367
Liquid-solid	0.8	32	40	0.0511	1.63395	0.4316
Liquid-solid	0.8	33	40	0.0495	1.63424	0.4342

TABLE IX. Uncertainties in surface free energy calculations. We give here all the contributions from what we identified as major sources of errors, for all our calculations grouped into categories of similar uncertainties. In the last column we give the final error bar that we associate with the calculations.

Calculation			Uncertainties on γ (units ε/σ^2)			
Lattice (plane)	Type	Temperatures	Length L_z	Spacing Δ	Parity N'_x	Total
FCC (111)	Liquid-solid	$0.8 \leq kT/\varepsilon \leq 2.0$	0.02	3×10^{-3}	3×10^{-3}	0.02
BCC (110)	Liquid-solid	$0.8 \leq kT/\varepsilon \leq 2.0$	0.02	3×10^{-3}	3×10^{-3}	0.02
BCC (111)	Vapor-solid	$0.1 \leq kT/\varepsilon \leq 0.3$	0.03	3×10^{-3}	0.02	0.04
Others	Liquid-solid	$0.8 \leq kT/\varepsilon \leq 2.0$	1×10^{-3}	3×10^{-3}	3×10^{-3}	4×10^{-3}
Others	Vapor-solid	$0.1 \leq kT/\varepsilon \leq 0.7$	1×10^{-3}	3×10^{-3}	0.02	0.02

contribution for the calculation of error bars. Instead, the difference between the discrete system and the exact limit of zero spacing can be appreciated in the main text figures by comparing the cDFT results to those of zero-temperature calculations.

Despite being satisfied with finite-spacing data, we still care however about the fact that the computational grid spacing is not exactly the same in all calculations. As explained in Appendix B 1, we choose the dimensions of the cell based on the equilibrium lattice constants of the solid at coexistence with the fluid. Because of this—and because the number of lattice points in the computational cell is an integer—we cannot choose a fixed grid spacing to use in all calculations. This should however be a minor concern since the deviations from the target spacing are about 1/30 of that spacing, and the errors due to the finite spacing are already quite small (about $0.1 \varepsilon/\sigma^2$). We thus expect small errors about $0.1/30 \approx 3 \times 10^{-3} \varepsilon/\sigma^2$ in magnitude.

The last major source of uncertainty is related to the parity of the number of points in the computational grid. Taking for example the cubic FCC cell, peaks located on the center of the cube faces will be centered on a site of the computational grid if the number of points is odd but not if it is even. For the narrow peaks of low-temperature calculations, this may have a noticeable effect on the calculation results. We estimate how much this affects the surface free energies we compute by performing two calculations with different number of lattice points for typical interfaces, which serves as benchmarks. Table VIII displays results of such calculations for both liquid-solid and vapor-solid interfaces. The effect is important (about $0.02 \varepsilon/\sigma^2$) in low-temperature vapor-solid calculations, since the solid peaks are very narrow and do not span over many

points in the computational grid. For that same reason it is less of a concern in liquid-solid calculations where the difference between results of two calculations with N and $N + 1$ lattice points is about $3 \times 10^{-3} \varepsilon/\sigma^2$. In this case we may argue that difference simply comes from the fact that the grid spacing is slightly different and not because of the parity in the number of lattice points.

A final concern one may have is that errors in the determination of bulk coexistence properties can propagate to the final result for the surface free energy. Indeed, we use a finite set of calculations and then interpolate the data several times first to compute bulk free energies along an isotherm and then again to find the coexistence point for that temperature. The result of these approximations is that the bulk properties we use to determine the surface free energy are not exactly the coexistence values. However, we have shown in Appendix B 6c that the surface free energy is only affected at second order by deviations from coexistence, i.e., proportionally to $(\mu - \mu_{\text{coex}})^2$, and these small inaccuracies can therefore be neglected.

All the contributions listed above along with the final uncertainties we associate with our calculations are displayed in Table IX. We report larger errors for some low-temperature BCC (111) calculations ($kT/\varepsilon \leq 0.3$) for which we attempted to stabilize the interface using the frozen bulk method. The method was not always successful with these profiles and we dispose of a limit amount of data to properly interpolate the minimum of the surface free energy $\gamma(N)$. We therefore reported the lowest values we got for the few properly stabilized interfaces, along with large error bars corresponding to the magnitude of variations between the valid calculations of lowest surface free energies.

- [1] D. Kashchiev, *Nucleation: Basic Theory with Applications* (Butterworth-Heinemann, Oxford, 2000).
- [2] M. Gallo, F. Magaletti, D. Cocco, and C. M. Casciola, Nucleation and growth dynamics of vapour bubbles, *J. Fluid Mech.* **883**, A14 (2020).
- [3] P. G. de Gennes, Wetting: Statics and dynamics, *Rev. Mod. Phys.* **57**, 827 (1985).
- [4] R. Evans, M. C. Stewart, and N. B. Wilding, A unified description of hydrophilic and superhydrophobic surfaces in terms of the wetting and drying transitions

- of liquids, *Proc. Natl. Acad. Sci. USA* **116**, 23901 (2019).
- [5] D. Seo, A. M. Schrader, S.-Y. Chen, Y. Kaufman, T. R. Cristiani, S. H. Page, P. H. Koenig, Y. Gizaw, D. W. Lee, and J. N. Israelachvili, Rates of cavity filling by liquids, *Proc. Natl. Acad. Sci. USA* **115**, 8070 (2018).
- [6] D.-K. Bučar, R. W. Lancaster, and J. Bernstein, Disappearing polymorphs revisited, *Angew. Chem. Int. Ed.* **54**, 317 (2008).
- [7] L. L. Zhang, S. Yang, W. Wei, and X. J. Zhang, Genetic polymorphisms affect efficacy and adverse drug reactions of

- DMARDs in rheumatoid arthritis, *Pharmacogenet. Genomics* **24**, 531 (2014).
- [8] S. L. Morissette, S. Soukasene, D. Levinson, M. J. Cima, and Ö. Almarsson, Elucidation of crystal form diversity of the HIV protease inhibitor ritonavir by high-throughput crystallization, *Proc. Natl. Acad. Sci. USA* **100**, 2180 (2003).
- [9] W. Cabri, P. Ghetti, G. Pozzi, and M. Alpegiani, Polymorphisms and patent, market, and legal battles: Cefdinir case study, *Org. Process Res. Dev.* **11**, 64 (2007).
- [10] H. G. Brittain, Theory and principles of polymorphic systems, in *Polymorphism in Pharmaceutical Solids*, edited by H. G. Brittain (Informa Healthcare, New York, 2009), pp. 1–23.
- [11] R. Lustig, On the Lennard-Jones and Devonshire theory for solid state thermodynamics, *Mol. Phys.* **115**, 1362 (2017).
- [12] J.-P. Hansen and I. McDonald, *Theory of Simple Liquids* (Academic Press, San Diego, 1986).
- [13] R. G. Parr and W. Yang, *Density-Functional Theory of Atoms and Molecules* (Oxford University Press, Oxford, 1989).
- [14] S. G. Wang, E. K. Tian, and C. W. Lung, Surface energy of arbitrary crystal plane of BCC and FCC metals, *J. Phys. Chem. Solids* **61**, 1295 (2000).
- [15] N. D. Mermin, Thermal properties of the inhomogeneous electron gas, *Phys. Rev.* **137**, A1441 (1965).
- [16] R. Evans, The nature of the liquid-vapour interface and other topics in the statistical mechanics of non-uniform, classical fluids, *Adv. Phys.* **28**, 143 (1979).
- [17] J. F. Lutsko, Recent developments in classical density functional theory, in *Advances in Chemical Physics* (John Wiley & Sons, Ltd., 2010), Chap. 1, pp. 1–92.
- [18] R. Roth, Fundamental measure theory for hard-sphere mixtures: A review, *J. Phys.: Condens. Matter* **22**, 063102 (2010).
- [19] H. Emmerich, H. Löwen, R. Wittkowski, T. Gruhn, G. I. Tóth, G. Tegze, and L. Gránásy, Phase-field-crystal models for condensed matter dynamics on atomic length and diffusive time scales: An overview, *Adv. Phys.* **61**, 665 (2012).
- [20] M. Oettel, S. Dorosz, M. Berghoff, B. Nestler, and T. Schilling, Description of hard-sphere crystals and crystal-fluid interfaces: A comparison between density functional approaches and a phase-field crystal model, *Phys. Rev. E* **86**, 021404 (2012).
- [21] J. F. Lutsko, Explicitly stable fundamental-measure-theory models for classical density functional theory, *Phys. Rev. E* **102**, 062137 (2020).
- [22] J. F. Lutsko and J. Lam, Classical density functional theory, unconstrained crystallization, and polymorphic behavior, *Phys. Rev. E* **98**, 012604 (2018).
- [23] J. F. Lutsko, How crystals form: A theory of nucleation pathways, *Sci. Adv.* **5**, eaav7399 (2019).
- [24] A. Härtel, M. Oettel, R. E. Rozas, S. U. Egelhaaf, J. Horbach, and H. Löwen, Tension and Stiffness of the Hard Sphere Crystal-Fluid Interface, *Phys. Rev. Lett.* **108**, 226101 (2012).
- [25] R. L. Davidchack, Hard spheres revisited: Accurate calculation of the solid-liquid interfacial free energy, *J. Chem. Phys.* **133**, 234701 (2010).
- [26] Y. Rosenfeld, Free-energy Model for the Inhomogeneous Hard-sphere Fluid Mixture and Density-functional Theory of Freezing, *Phys. Rev. Lett.* **63**, 980 (1989).
- [27] J. F. Lutsko and C. Schoonen, Classical density-functional theory applied to the solid state, *Phys. Rev. E* **102**, 062136 (2020).
- [28] J. Guénoilé, W. G. Nöhring, A. Vaid, F. Houllé, Z. Xie, A. Prakash, and E. Bitzek, Assessment and optimization of the fast inertial relaxation engine (FIRE) for energy minimization in atomistic simulations and its implementation in LAMMPS, *Comput. Mater. Sci.* **175**, 109584 (2020).
- [29] We use the terms surface tension and interfacial or surface free energy as synonyms. Surface tension is a term that is also sometimes used to refer to another quantity called the surface stress. There is no ambiguity with vapor-liquid interfaces where these two quantities are identical, but it is not the case with solids [43,44]. Here we never mean the surface stress.
- [30] M. Maeritz and M. Oettel, Density functional for the lattice gas from fundamental measure theory, *Phys. Rev. E* **104**, 024124 (2021).
- [31] F. Turci, T. Schilling, M. H. Yamani, and M. Oettel, Solid phase properties and crystallization in simple model systems, *Eur. Phys. J.: Spec. Top.* **223**, 421 (2014).
- [32] H. Hansen-Goos and R. Roth, Density functional theory for hard-sphere mixtures: The White Bear version mark II, *J. Phys.: Condens. Matter* **18**, 8413 (2006).
- [33] G. Grimvall, B. Magyari-Köpe, V. Ozoliņš, and K. A. Persson, Lattice instabilities in metallic elements, *Rev. Mod. Phys.* **84**, 945 (2012).
- [34] J. Q. Broughton and G. H. Gilmer, Molecular dynamics investigation of the crystal-fluid interface. IV. Free energies of crystal-vapor systems, *J. Chem. Phys.* **84**, 5741 (1986).
- [35] A. Travesset, Phase diagram of power law and Lennard-Jones systems: Crystal phases, *J. Chem. Phys.* **141**, 164501 (2014).
- [36] P. Grosfils and J. F. Lutsko, Dependence of the liquid-vapor surface tension on the range of interaction: A test of the law of corresponding states, *J. Chem. Phys.* **130**, 054703 (2009).
- [37] B. B. Laird, R. L. Davidchack, Y. Yang, and M. Asta, Determination of the solid-liquid interfacial free energy along a coexistence line by Gibbs-Cahn integration, *J. Chem. Phys.* **131**, 114110 (2009).
- [38] J. P. Tipseev, A. O. Rino and E. D. Zanotto, Direct determination of Lennard-Jones crystal surface free energy by a computational cleavage method, *J. Chem. Phys.* **155**, 094101 (2021).
- [39] H. Childs, E. Brugger, B. Whitlock, J. Meredith, S. A. and Kathleen Bonnell, M. Miller, G. H. Weber, C. Harrison, D. Pugmire, T. Fogal, C. Garth, A. Sanderson, E. W. B. and Marc Durant, D. Camp, J. M. Favrek, O. Rubel, P. Navratil, M. Wheeler, P. Selby, and F. Vivodtzev, Visit: An end-user tool for visualizing and analyzing very large data, in *High Performance Visualization: Enabling Extreme-Scale Scientific Insight*, edited by E. Bethel, H. Childs, and C. Hansen (Taylor & Francis, Boca Raton, FL, 2013), pp. 357–372.
- [40] N. Krainyukova, On the mechanism of the BCC-HCP transformations in small Lennard-Jones crystals, *J. Low Temp. Phys.* **150**, 317 (2008).
- [41] W. C. Swope and H. C. Andersen, 10^6 -particle molecular-dynamics study of homogeneous nucleation of crystals in a supercooled atomic liquid, *Phys. Rev. B* **41**, 7042 (1990).
- [42] C. Schoonen and J. F. Lutsko, Crystal Polymorphism Induced by Surface Tension, *Phys. Rev. Lett.* **129**, 246101 (2022).
- [43] R. Shuttleworth, The surface tension of solids, *Proc. Phys. Soc. A* **63**, 444 (1950).

- [44] N. Di Pasquale and R. L. Davidchack, Shuttleworth equation: A molecular simulations perspective, *J. Chem. Phys.* **153**, 154705 (2020).
- [45] D. Chandler and J. D. Weeks, Equilibrium Structure of Simple Liquids, *Phys. Rev. Lett.* **25**, 149 (1970).
- [46] J. D. Weeks, D. Chandler, and H. C. Andersen, Role of repulsive forces in determining the equilibrium structure of simple liquids, *J. Chem. Phys.* **54**, 5237 (1971).
- [47] H. C. Andersen, J. D. Weeks, and D. Chandler, Relationship between the hard-sphere fluid and fluids with realistic repulsive forces, *Phys. Rev. A* **4**, 1597 (1971).
- [48] J. A. Barker and D. Henderson, Perturbation theory and equation of state for fluids. II. A successful theory of liquids, *J. Chem. Phys.* **47**, 4714 (1967).
- [49] A. Stukowski, Visualization and analysis of atomistic simulation data with OVITO—The open visualization tool, *Modell. Simul. Mater. Sci. Eng.* **18**, 015012 (2010).